PCCP

ROYAL SOCIETY OF CHEMISTRY

PAPER

View Article Online
View Journal | View Issue

Cite this: *Phys. Chem. Chem. Phys.*, 2022, **24**, 7007

Pressure tuned incommensurability and guest structure transition in compressed scandium from machine learning atomic simulation†

Sheng-cai Zhu, ‡*[a] Zhen-bo Huang,‡[a] Qingyang Hu [bc] and Liang Xu[d]

Received 20th December 2021,
Accepted 21st February 2022

DOI: 10.1039/d1cp05803g

rsc.li/pccp

Scandium (Sc) is the lightest non-main-group element and transforms to a host–guest (H–G) incommensurate structure under gigapascal (GPa) pressures. While the host structure is stable over a wide pressure range, the guest structure may exist in multiple forms, featuring different incommensurate ratios, and mixing up to generate long-range "disordered" guest structures. Here, we employed the recently developed global neural network (g-NN) potential and the stochastic surface walking (SSW) global optimization algorithm to explore the global potential energy surface of Sc under various pressures. We probe the global minima structure in a system made of hundreds of atoms and revealed that the solid-phase transition between Sc-I and H-G Sc-II phases is fully reconstructive in nature. Above 62.5 GPa, the pressure will further destabilize the face-centered tetragonal (fct, Sc-IIa) guest structure to a body-centered tetragonal phase (bct, Sc-IIb), while sustaining the host structure. The structural transition mechanism of this work will shed light on the nature of the complex H–G structural modifications in compressed metals.

1. Introduction

Atoms of single element metals are often packed in high symmetry under ambient conditions, whereas a specific group of metals may transition to a complex incommensurate structure that comprises interpenetrating host and guest (H–G) components under pressure. The guest structures are chains of atoms filling the channels of the host structure, often along the longer c axis.[1,2] As a measure of the H–G structure, the incommensurate ratio γ is defined as c_h/c_g, where c_h and c_g are the c axis length of host and guest structures, respectively. The intriguing structural complexity has led to experimental and theoretical discoveries of incommensurate phenomena on a variety of metals.[3–5] To date, the H–G structures have been found in nine elements, namely Ba, Sr, Sc, Ca, As, Sb, Bi, Rb and K.[2,6–8] However, due to the enlarged lattice size and sophisticated atomic packing, our knowledge on the structural characterization and transitions in H–G structures is still sketchy. We are facing three challenges in probing the H–G structures: (i) the exact incommensurate ratio γ,[9] (ii) the guest configuration,[1,2,7–11] and (iii) the transition mechanism from the simple high symmetry phase to the complex H–G structure under high pressure.

The ambient stable Sc (hcp, Sc-I) transforms to an incommensurate structure above 23 GPa. It has attracted special interest[12–22] since the single element Sc features one of the highest superconducting transition temperatures T_c in the periodic table,[16] and T_c increases to ~19.6 K by applying an external pressure in incommensurate Sc-II.[13,18] A snapshot of Sc-II shows that its host framework is made of a tetragonal lattice with 8 atoms.[23] However, the guest structure is controversial. Fujihisa *et al.*[24] proposed that the guest structure has a body-centered tetragonal (bct) lattice with an anomalously short interatomic distance in the guest atomic chains. Later, using the monochromatic synchrotron XRD technique, McMahon *et al.*[11] found that the guest structure with a face-centered tetragonal (fct) lattice fits better. Ormeci *et al.*[12] employed first-principles simulation and explained that the discrepancy stems from the lower energy of the fct guest structure (superspace group $I4/mcm(00\gamma)$) than the body-centered tetragonal guest structure (superspace group $I4/mcm(00\gamma)$). Varying the incommensurate ratio, Arapan *et al.*[25] constructed a series of Sc-II crystal structures with difference γ (3/2, 4/3, 5/4, 6/5, 10/7, and 14/11) and suggested that those with γ = 14/11 and 4/3 have

[a] *School of Materials, Shenzhen Campus of Sun Yat-sen University, Shenzhen 518107, China. E-mail: zhushc@mail.sysu.edu.cn*
[b] *Center for High Pressure Science and Technology Advanced Research, Beijing 100094, P. R. China*
[c] *CAS Center for Excellence in Deep Earth Science, Guangzhou Institute of Geochemistry, Chinese Academy of Sciences, Guangzhou, P. R. China*
[d] *National Key Laboratory of Shock Wave and Detonation Physics, Institute of Fluid Physics, China Academy of Engineering Physics, Mianyang 621900, China*

† Electronic supplementary information (ESI) available: The phase transition IS/FS pairs. See DOI: 10.1039/d1cp05803g

‡ These authors contributed equally: Sheng-cai Zhu, Zhen-bo Huang.

relatively lower energies. In other incommensurate metals, for example Ba-IV, McMahon *et al.* found[1] that the fct guest lattice transitions to a face-centered monoclinic (fcm) lattice at 12.6 GPa and then to a two-dimensional pattern with disordered guest–atom chains at 19 GPa.[26] The study showed that the guest structure can follow the symmetries of fct, fcm and even the ''disordered'' guest structure. It was worth noting that the stability pressure range of Sc-II spans over 80 GPa (from 23 to 104 GPa),[23] which is much wider than those of other incommensurate structures (*e.g.* Ba and Sr). However, the nature of the large pressure stability range of Sc-II is still unknown.

The structural complexity of the incommensurate structure is a major challenge for exhaustive first-principles simulations. Taking the fct (γ = 14/11) guest lattice Sc-II as an example, there are 116 atoms in the tetragonal supercell (88 host atoms and 28 guest atoms). To date, it has been beyond the capability of first-principles simulation to construct the entire high-pressure potential energy surface. To ensure speed and calculation accuracy, we for the first time developed a machine learning potential[27] for the high-pressure Sc system, namely, the Sc global neural network (g-NN) potential, which is $\sim$4 orders faster[28] than density functional theory while maintaining sufficient precision in calculating energies. Using the stochastic surface walking (SSW)[29–31] global optimization based on the g-NN potential, we found that the fct guest lattice transited to the bct lattice when the pressure is above 56 GPa. Using SSW pathway sampling, we identified a preferred transition pathway from Sc-I to Sc-II, along which the atomic structure is reconstructed in the recrystallization mechanism. A similar transition mechanism can readily be applied to other metals with incommensurate structures.

2. Methods

2.1 SSW global optimization and pathway sampling

The SSW global optimization[29–31] was implemented in the package of large-scale atomic simulation with the neural network potential (LASP, webpage www.lasphub.com).[32] In the SSW method, the movement on the potential surface is guided by the random soft mode (a second derivative) direction, which is capable of exploring both novel structures and reaction pathways exhaustively and unbiasedly. By combining SSW with the global neural network potential[27] (described below), we are able to map the complex potential energy surface (PES) of Sc.

The solid-phase transition mechanism between Sc-I (hcp) and Sc-II was investigated by the SSW–NN method. Through SSW–NN sampling, a large set (in the order of 10^3) of the initial state and final state (IS/FS) pairs was collected at 30 GPa, including the lowest energy barrier pathways. The transition state of the possible pathways was located by using the variable-cell double-ended surface walking (VC-DESW)[31] approach and refined by sorting the heights of computed energy barriers. Then, pathways with lowest energies will be further calculated by calculations on the basis of density functional theory (DFT) to obtain the accurate energetic barrier of the reaction. This method has successfully been used to predict the low-energy pathways of crystal phase transitions, such as the free energy landscape of carbon allotropes.[33,34]

2.2 High-pressure Sc g-NN potentials

The g-NN potential is generated using the SSW–NN method, which is now implemented using the LASP software. The g-NN potential is obtained by self-machine learning of the DFT data set by minimizing the difference between the NN and DFT results on the total energy, interatomic force, and lattice stress. In this work, the representative first-principles data set was generated by SSW global optimization, covering pressures of 0, 30, 60, 90, 120, 150 and 180 Gpa. The data set is calculated using the Vienna *ab initio* simulation package with high accuracy criterions[35] (see below). The typical procedure and the hyperparameters utilized in the g-NN training can be found in recent publications.[27] In each cycle, the g-NN potential is tested with a newly generated structure from SSW. More than 10^7 structures on the high-pressure Sc PES were observed by SSW–NN during the generation process and the final training data set of Sc consists of 5558 structures to represent the global PES. The g-NN follows the feed-forward NN architecture with five layers (212-60-50-50-1), with 18 643 fitting parameters consisting of 91 two-body, 93 three-body and 12 four-body descriptors. For the final g-NN potential, the root-mean-square errors for the energy and force reach 4.181 meV per atom and 0.114 eV Å^{-1}, respectively. The validation of the NN potential is found in Table 1. This g-NN potential is currently included in the g-NN library of LASP (accessible from the LASP webpage). We have also benchmarked the g-NN accuracy against the DFT results for important structures, which show that the energy root-mean-square is no more than 4 meV per atom for low energy structures and pathways in this work. The benchmarked high accuracy of the g-NN PES suggests that it is a good approximation to the DFT PES, which can be utilized to expedite the global structure search and pathway determination.

Table 1 Relative energy (DFT and NN) and lattice configuration of 10 lowest energy structures at 30 GPa. Str-1 is the global minimum (GM), both the DFT and NN energies were set to zero. The last column lists the Sc–Sc bond distance

		DFT	NN			Sc–Sc (Å)	
Number	Symmetry	(eV per atom)	(eV per atom)	Guest structure	γ	Host	Guest
Str-1	$P\bar{1}$	0	0	fcm	1.247	3.327	2.623
Str-2	$I4/mcm$	0.004	0.002	fct	1.332	3.352	2.516
Str-3	$C2/m$	0.005	0.002	fcm	1.333	3.356	2.517
Str-4	Cc	0.01	0.012	bcm	1.198	3.248	2.710
Str-5	$P6_3/mmc$	0.012	0.013	—	—	2.928[a]	
Str-6	$R\bar{3}m$	0.014	0.014	—	—	2.927[a]	
Str-7	$P\bar{1}$	0.014	0.013	bcm	1.169	3.275	2.802
Str-8	$P6/mmm$	0.015	0.016	—	—	2.808[a]	
Str-9	$R32$	0.021	0.013	—	—	2.884[a]	
Str-10	$P6_3/mmc$	0.022	0.021	—	—	2.880[a]	

[a] The Sc–Sc distance is for the shortest distance.

2.3 DFT calculations

The g-NN potential training relies heavily on the DFT calculated energy, forces and stresses of structures. To achieve the high accuracy and data consistency, our DFT calculations were performed in the plane wave density functional theory program and organized by a module in the generation of the LASP g-NN library. The electron–ion interactions of the Sc atom are represented by the projector augmented wave scheme.[36] To describe the electronic structure of different Sc phases under high pressures, the Sc potential with $3s^2 3p^6 3d^1 4s^2$ valence orbitals was used. The exchange–correlation functional is described by the generalized gradient approximation in Perdew–Burke–Ernzerhof parameterization.[37] The kinetic energy cutoff is 450 eV. The fully automatic Monkhorst–Pack *K*-mesh with 25 times the reciprocal lattice vectors was used for the Brillouin zone *k*-point sampling.[38] The geometry convergence criterion was set as 0.001 eV Å^{-1} for the maximal component of force and 0.01 GPa for lattice stress.

3. Results

3.1 The Sc global PES at 30 GPa

First, we explored the Sc PES at 30 GPa using the SSW–NN method. More than 500 000 minima were sampled using different sizes of the supercell with up to 48 atoms. After removing the identical structural isomers, we finally obtained 16 610 distinct structures. The lowest energy 10 structures were further investigated by DFT. Table 1 shows the energy from DFT and NN calculations. We plotted the total energy against the structural order parameter, the Steinhart-order parameter with degree $l = 2$ (OP_2),[39] as shown in Fig. 1a. The density of states (DOS) is visualized by color gradients in the two-dimensional PES. The higher DOS means the greater probability to find energetically degenerate structures with similar structural patterns.

At 30 GPa, we found the global minimum of Sc is located at a H–G structure with the fcm guest structure, which contradicts with the experimental fct-type Sc-II.[11] The inconsistence between the experiment and the present calculation may be due to an insufficient supercell size in simulation. It is well known that the H–G structure is extremely complex; both the commensurate ratio and guest configuration will influence the energy. For example, the bct configuration with the guest configuration $\gamma = 14/11$ has a lower energy than the fct configuration with the guest configuration $\gamma = 10/7$ (see the following content). However, lacking periodicity in the *c* direction, the huge system (the truly incommensurate structure exhibits a large supercell) PES searching is beyond our calculation capability. We also found that the global minimum is surrounded by minima with close energies (Fig. 1). It is worth mentioning that their energies were cross-checked by DFT calculations and we have reached an excellent agreement between NN and DFT. On the PES, six representative low energy minima were highlighted with symbols in Fig. 1a, namely Str-1 to Str-5, and Str-10 sorted by the descending energy, in which Str-1 to Str-4 are H–G isostructures (Fig. 1b), while Str-5 is a double hexagonal-close-packed (dhcp) structure and Str-10 is Sc-I with the hcp structure, which is not shown. The highly ranked H–G structures are consistent with experiments in which Sc forms the H–G structure under compression. Our results confirmed that all H–G structures have close energies. However, they feature very different Steinhart order parameters, indicating that they have a distinct local atomic environment, which originates from different guest configurations and commensurate ratios. Specifically, their guest structures took the configurations of fcm, fct, fcm and body-centered-monoclinic (bcm), respectively, and the incommensurate ratio ranged from 1.169 to 1.333.

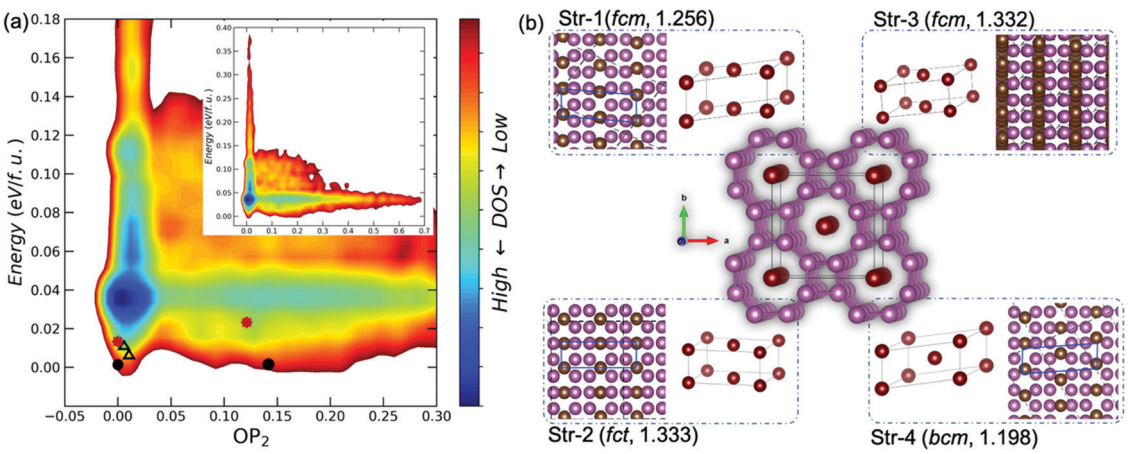

Fig. 1 (a) Global PES for filtered low energy structures using the $OP_2 \sim E$ contour plot. The main figure is enlarged from the inset covering the full energy range from the SSW–NN PES data. OP_2: the structure order parameter with $l = 2$. Structures below are labelled by black dots and triangles with coordinates (OP_2, E): black dots, Str-1(0.0062, 0) and Str-2 (0.1428, 0.002); black hollow triangles, Str-3 (0.0137, 0.002) and Str-4 (0.0089, 0.011); and red stars, Str-5(0.0065, 0.013) and Str-10 (0.1190, 0.022). (b) Atomic structures of Str-1, Str-2, Str-3 and Str-4, and the H–G structure. The incommensurate ratios are indexed after the abbreviated guest structure type. Symbols: pink ball, Sc of the host structure; grey ball, Sc of the guest structure.

Other than the H–G structure, the global PES is made up of a large, smeared DOS zone, where the structures generally have higher energies but they are frequently observed by our structural searching algorithm. According to the energy landscape theory,[40] all the structures were unbiasedly sampled; given the relative lower energy of the higher DOS zone, it is possible that these structures will be the structural intermediates on the transition pathway from Sc-I to Sc-II, as the amorphous phase.

We also constructed the same PES at 90 GPa, which is shown in Fig. S1 in the ESI.† In addition to our previous work,[41] SSW–NN enabled much extensive structural search and the global minima structure of the Ccca-type phase eventually reached an agreement with the experiment,[41] which is not the $P4_12_12$ structure.[42] By comparing the energy, we found that the $P4_12_12$ structure has a higher energy than the *Ccca* structure. Additionally, the simulated XRD of the $P4_12_12$ structure is inconsistent with the experiment. Among the lowest energy structures, there are two H–G structures whose energies are only 12–14 meV per atom above the *Ccca* structure. Their host structures and guest structures are distorted, while the whole H–G structures are similar to Sc-II at 30 GPa. The distortion of the host and guest structure helps in reducing local stress. Such modulations have been found in Ca-VII at 210 GPa[3] and S at 400 GPa.[43]

3.2 Variation of the guest structure in Sc-II

The coupling of the incommensurate ratio γ to the guest configuration would form a new H–G structure. First, we generated a series of structures with γ of 3/2, 10/7, 4/3, 14/11, 5/4, and 6/5 (as shown in Fig. S2a, ESI†) and calculated their energies. Then, we change the guest tetragonal lattice to the monoclinic lattice, namely fcm, bcm and even the bct guest configuration with γ = 14/11. The departure from tetragonal is defined by the deviation angle (β). For convenience, we use τ, which defined as L_a/L_cT (L_a is the length of the supercell in a direction, L_c is the shift distance in the c direction, and T is T_a/T_c, see Fig. S3, ESI†), to measure this deviation. Here, each guest configuration (fct, fcm and bcm) H–G structure contains several structures (τ from 1 to 6). The enthalpies for all of the H–G structures as a function of pressure (from 25 to 80 GPa) are plotted in Fig. 2a and b. For both fct and bct, H–G structures with γ = 14/11 have the lowest energies. However, the energy of the bct configuration decreases abruptly at above 35 GPa. Consequently, bct with γ = 14/11 and 5/4 became energetically favorable at 50 GPa. Here, *via* systematic research, we suggest that Sc-II will undergo the guest structure phase transition to the bct configuration when the pressure is above 50 GPa.

Fig. 2c plotted the energy *vs.* γ for the bct and fct guest configurations at 30 GPa (60 GPa results are shown in Fig. S3c, ESI†). The energy of the bct configuration (Fujihisa's model) is higher than that of the fct configuration (McMahon's model) with the same commensurate ratio at a pressure range of 25–50 GPa, which is consistent with Ormeci.[12] However, at above 60 GPa, a high γ (>14/11) range in the bct guest becomes more energetically favored. Our results suggest that the energy of the H–G structure is influenced by both the incommensurate ratio γ and guest configuration. From Fig. 2c, we can find that, in fct and bct guest configuration H–G structures, the optimal value of γ under different pressures (30 and 60 GPa) is 14/11.

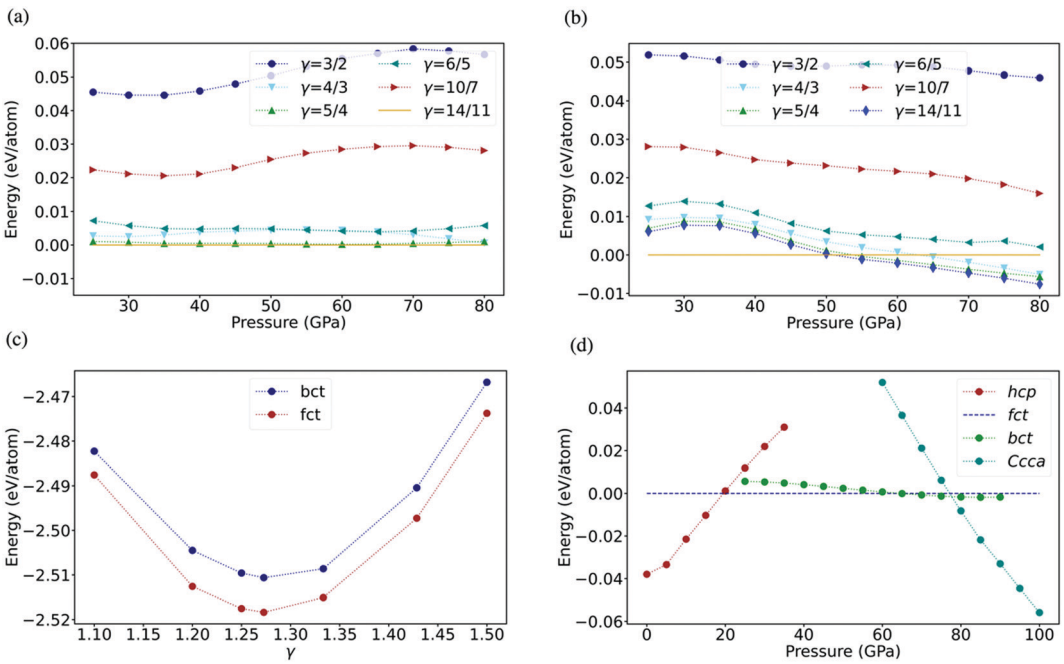

Fig. 2 (a) Relative energies of the fct guest configuration as a function of pressure (relative to γ = 14/11 of fct). (b) Relative energies of the bct guest configuration as a function of pressure (relative to γ = 14/11 of fct). (c) Energies *vs.* γ at 30 GPa. (d) Relative energies of hcp and Sc-II with bct (γ = 14/11) and Ccca structures as a function of pressure (relative to the fct 14/11 structure).

As shown in Fig. S3 in the ESI,† a series of structures (τ = 1, 2, 3, 4, 5, and 6) in the *fcm* guest configuration were constructed. It should be noticed that *bct* and *fct* are two terminals in these guest configurations, namely τ = 1 is the *bct* configuration, while τ = ∞ is the *fct* configuration, see Fig. S3a (ESI†). With τ increasing from 1 to 6, the unit cell increases from 116 atoms to 696 atoms, which is beyond the capability of DFT. The energy of *fcm* with *fct* as the reference, calculated by the neural network potential, is shown in Fig. S3d (ESI†). We can find that the energies decrease monotonically with the increase of τ (β decreasing) at 30 and 40 GPa. At 50 GPa, τ has a negligible effect on the energy. While at 60 and 70 GPa, bct becomes energetically favorable. This one step further confirms that the *bct* configuration is energetically favorable when the pressure is above 60 GPa.

In order to confirm the NN results, we calculate the energies of fct (14/11) and bct (14/11) configurations by DFT. For comparison, the energies of hcp and the Ccca structure are also calculated. As shown in Fig. 2d, fct (14/11) becomes energetically favorable at ∼20 GPa, which is consistent with the experiment that Sc-I transitions to Sc-II at ∼23 GPa. Comparing with fct (14/11), the energy of the H–G structure with bct guest structures decreases as the pressure increases and becomes the favorable structure above ∼62.5 GPa. When the pressure is above 77.5 GPa, the Ccca structure becomes the most stable phase. Though the DFT results show 12.5 Gpa higher than the NN prediction, it confirms that the H–G structure with the bct guest configuration has a lower energy than that with the fct one. It is safe to conclude that the guest structure undergoes a transition from fct (named Sc-IIa) to bct (named Sc-IIb) before the Sc-II transition to Sc-III at 107 GPa. This also may explain that the Sc-II with the fct structure is unstable above 60 GPa by DFT calculations.[25] This can also well interpret the wide pressure stable range of Sc-II.

3.3 The transition mechanism from Sc-I to Sc-II

Sc-I to Sc-II represents an important phase transition type from hcp to the incommensurate phase. Here, we use the 42-atom cell with $\gamma = 1.241$ and 32-atom cell with $\gamma = 1.331$ to sample the phase transition pathway between Sc-I and the H–G phase. By using the SSW sampling method, more than 5×10^3 pairs of initial and final states were obtained. The low energy reaction quasi-pathways were obtained using the DESW method. Finally, we refined the pathway by DFT calculations. As the energy profile showed in Fig. 3a, we can find that the lowest energy pathway (42-atom unit cell) has a reaction barrier of 32.0 meV per atom from DFT calculations (compared to 35 meV per atom from NN). In contrast, the reaction barrier in the 32-atom unit cell pathway is 44 meV per atom from DFT calculations (40 meV per atom for NN). Both phase transition energy barriers are relatively low, which indicates that the Sc-I (hcp) to Sc-II (H–G) solid phase transition can occur at room temperature.

In addition to the reaction profile, Fig. 3b also shows the atomistic transition mechanism of the phase transition. Both pathways are linked by two monoclinic lattices. Along the 42-atom path, the closely packed $(001)_I$ plane is fluctuating

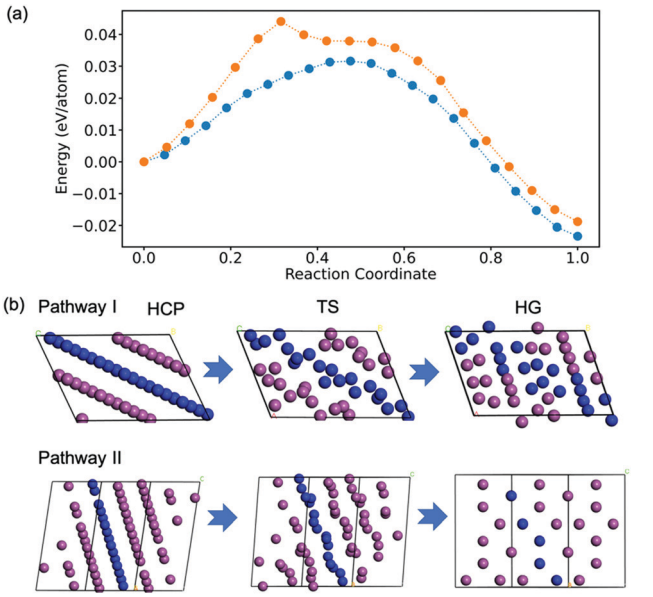

Fig. 3 (a) Energy barriers of two transition pathways from DFT calculations: 42-atom (Pathway I): blue; 32-atom (Pathway II): orange. (b) Structural snaps during the phase transition paths.

into the atom band without a notable plane. While in the 32-atom path, the close packed $(001)_I$ plane evolves into the $(310)_{II}$ plane. We note that there is no definite orientation relationship between Sc-I and Sc-II analyzed by the phenomenological theory of Martensitic crystallography (PTMC).[44] The presence of the orientation relationship was known to be an important feature in the martensitic phase transition, where the phase transition involves the collective movement during the phase transition.

Here, the transition from Sc-I to Sc-II is manifested by atomic reconstruction with a negligible shearing movement (more in the animation of the ESI†). From the crystallography perspective, the one-to-one correspondence for the lattice ($L(e_1, e_2, e_3)$, e_i being the lattice vector) and atom ($q_i, \ldots, q_N$) from one crystal phase to another is defined by the reaction coordinates of $Q_{IS}(L, q) \rightarrow Q_{FS}(L, q)$.[45] In the incommensurate structure, it is not possible to define the same $Q_{IS}(L, q) \rightarrow Q_{FS}(L, q)$ in the simple crystal because the incommensurate structure used an approximant periodic analogue. As a result, the atom movement pattern would change once the γ changed. For example, in the pathway II, the closely packed (001) plane cannot transition into the $(310)_{II}$ plane if the incommensurate ratio γ changed. The presence of a structurally "disordered" guest sublattice (varying with pressure), a key characteristic of the H–G structure, would change the phase transition mechanism. For example, in the 48-atom pathway, see Fig. S4 (ESI†), two low symmetry intermediate structures are on the pathway of Sc-I to Sc-II. In the context with experimental findings, the reconstructive mechanism with the crystal–amorphous–crystal path can well explain the Akahama[23] experiment, where Sc-I to Sc-II was found in the recrystallization mechanism.

3.4 Discussion

In this work, we further constrain the phase stability field of Sc under high pressures (Table 2). Under hydrostatic pressures,

Table 2 Phase stability fields of Sc under high pressures

Phase	Pressure (GPa)	Number	Symmetry group
Sc-I	0–23	194	$P6_3/mmc$
Sc-II	23–63		Host: $I4/mcm$ Guest: fct
	63–104[a]	104	Host: $I4/mcm$ Guest: bct
Sc-III	104–140	68[b]	*Ccca*
Sc-IV	140–240	64[b]	*Cmca*
Sc-V	>240	178[c]	$P6_122$

[a] The transition pressures of Sc-II to Sc-III are 104 GPa from the experiment and ~75 GPa from DFT calculations. [b] No experimental structure data for Sc-III and Sc-IV. [c] Structure information from ref. 23.

Sc-I transitions to H–G Sc-II at 23 GPa, but the stable pressure range of Sc-II (23–104 GPa) will decompose into two segments. In between 23 and 62.5 GPa, the guest configuration of H–G Sc-II is fct, and then it transitions to the bct guest configuration with the host configuration remaining unchanged. We further predicted that at higher pressures, *e.g.* above 104 GPa, in the experiment (75 GPa from DFT calculations), Sc-II transitions to Sc-III. Although the atomic structure of the Sc-III phase has not yet been solved by experiments, our work proposed that Ccca would be the stable Sc-III phase. We also predicted the crystal of Sc (Sc-IV) at a megabar pressure, although they need more experimental studies to verify.

4. Conclusions

In summary, we developed an accurate global NN potential for single element Sc and performed extensive SSW-NN global optimization to collect the global PES data under high pressure. We identified a set of subtle guest structural transitions in Sc-II, which would be responsible for the wide stability pressure range of Sc-II. The indefinite one-to-one correspondence for the lattice and the atom in hcp to the H–G phase transition mechanism will shed light on the nature of the incommensurate structure in a variety of single element metals.

Author contributions

Sheng-cai Zhu conceived the research idea, Sheng-cai Zhu and Zhen-bo Huang performed the calculations and analyzed the simulation data. Sheng-cai Zhu, Zhen-bo Huang and Qing-yang Hu wrote and revised the manuscript.

Conflicts of interest

The authors declare no competing financial interests.

Acknowledgements

S. C. Z. is supported by the National Natural Science Foundation of China (Grant No. 21703004) and the Hundreds of Talents Program of Sun Yat-sen University. Q. Y. H. is supported by the CAEP Research Project (CX20210048) and a Tencent Xplore prize. We thank Zhi-Pan Liu for helping in constructing the Sc-NN potential. We also acknowledge the use of computing resources from Tianhe-2 Supercomputer.

References

1 R. J. Nelmes, D. R. Allan, M. I. McMahon and S. A. Belmonte, Self-hosting incommensurate structure of barium IV, *Phys. Rev. Lett.*, 1999, **83**(20), 4081–4084.
2 M. I. McMahon, O. Degtyareva and R. J. Nelmes, Ba-IV-Type incommensurate crystal structure in group-V metals, *Phys. Rev. Lett.*, 2000, **85**(23), 4896–4899.
3 H. Fujihisa, Y. Nakamoto, M. Sakata, K. Shimizu, T. Matsuoka, Y. Ohishi, H. Yamawaki, S. Takeya and Y. Gotoh, Ca-VII: A chain ordered host-guest structure of calcium above 210 GPa, *Phys. Rev. Lett.*, 2013, **110**(23), 235501.
4 A. R. Oganov, Y. Ma, Y. Xu, I. Errea, A. Bergara and A. O. Lyakhov, Exotic behavior and crystal structures of calcium under pressure, *Proc. Natl. Acad. Sci. U. S. A.*, 2010, **107**(17), 7646–7651.
5 M. I. McMahon and R. J. Nelmes, High-pressure structures and phase transformations in elemental metals, *Chem. Soc. Rev.*, 2006, **35**(10), 943–963.
6 M. I. McMahon, O. Degtyareva, R. J. Nelmes, S. Van Smaalen and L. Palatinus, Incommensurate modulations of Bi-III and Sb-II, *Phys. Rev. B: Condens. Matter Mater. Phys.*, 2007, **75**(18), 184114.
7 O. Degtyareva, M. I. McMahon and R. J. Nelmes, Pressure-induced incommensurate-to-incommensurate phase transition in antimony, *Phys. Rev. B: Condens. Matter Mater. Phys.*, 2004, **70**(18), 184119.
8 M. I. McMahon, R. J. Nelmes, U. Schwarz and K. Syassen, Composite incommensurate K-III and a commensurate form: Study of a high-pressure phase of potassium, *Phys. Rev. B: Condens. Matter Mater. Phys.*, 2006, **74**(14), 140102.
9 M. I. McMahon, S. Rekhi and R. J. Nelmes, Pressure dependent incommensuration in Rb-IV, *Phys. Rev. Lett.*, 2001, **87**(5), 055501.
10 M. Mcmahon, T. Bovornratanaraks and D. R. Allan, Observation of the incommensurate barium-IV structure in strontium phase V PXRD crystal structure determination view project physics of metal hydrides view project, *APS*, 2000, **61**(5), 3135–3138.
11 M. I. McMahon, L. F. Lundegaard, C. Hejny, S. Falconi and R. J. Nelmes, Different incommensurate composite crystal structure for Sc-II, *Phys. Rev. B: Condens. Matter Mater. Phys.*, 2006, **73**(13), 134102.
12 A. Ormeci, K. Koepernik and H. Rosner, First-principles electronic structure study of Sc-II, *Phys. Rev. B: Condens. Matter Mater. Phys.*, 2006, **74**(10), 104119.
13 J. J. Hamlin and J. S. Schilling, Pressure-induced superconductivity in Sc to 74 GPa, *Phys. Rev. B: Condens. Matter Mater. Phys.*, 2007, **76**(1), 012505.
14 J. Wittig, C. Probst, F. A. Schmidt and K. A. Gschneidner Jr, Superconductivity in a new high-pressure phase of scandium, *Phys. Rev. Lett.*, 1979, **42**(7), 469.

15 R. Briggs, M. G. Gorman, A. L. Coleman, R. S. McWilliams, E. E. McBride, D. McGonegle, J. S. Wark, L. Peacock, S. Rothman and S. G. Macleod, *et al.*, Ultrafast X-ray diffraction studies of the phase transitions and equation of state of scandium shock compressed to 82 GPa, *Phys. Rev. Lett.*, 2017, **118**(2), 1–6.
16 M. Debessai, J. J. Hamlin and J. S. Schilling, Comparison of the pressure dependences of T_c in the trivalent D-electron superconductors Sc, Y, La, and Lu up to megabar pressures, *Phys. Rev. B: Condens. Matter Mater. Phys.*, 2008, **78**(6), 64519.
17 S. K. Bose, Linear response results for phonons and electron–phonon coupling in hexagonal close packed Sc-spin fluctuations, and implications for superconductivity, *J. Phys.: Condens. Matter*, 2008, **20**(4), 45209.
18 Y. K. Vohra, W. Grosshans and W. B. Holzapfel, High-pressure phase transformation in scandium, *Phys. Rev. B: Condens. Matter Mater. Phys.*, 1982, **25**(9), 6019–6021.
19 Y. Zhao, F. Porsch and W. Holzapfel, Evidence for the occurrence of a prototype structure in Sc under pressure, *Phys. Rev. B: Condens. Matter Mater. Phys.*, 1996, **54**(14), 9715–9720.
20 A. M. Molodets, D. V. Shakhray, A. A. Golyshev and V. E. Fortov, Electrophysical and thermodynamic properties of shock compressed incommensurate phase Sc-II, *Phys. Rev. B: Condens. Matter Mater. Phys.*, 2007, **75**(22), 224111.
21 H. Olijnyk, S. Nakano, A. P. Jephcoat and K. Takemura, Unusual pressure response of the E2g mode and elastic shear modulus C44 in Hcp scandium, *J. Phys.: Condens. Matter*, 2006, **18**(48), 10971.
22 L. W. Nixon, D. A. Papaconstantopoulos and M. J. Mehl, Calculations of the superconducting properties of scandium under high pressure, *Phys. Rev. B: Condens. Matter Mater. Phys.*, 2007, **76**(13), 134512.
23 Y. Akahama, H. Fujihisa and H. Kawamura, New helical chain structure for scandium at 240 GPa, *Phys. Rev. Lett.*, 2005, **94**(19), 195503.
24 H. Fujihisa, Y. Akahama, H. Kawamura, Y. Gotoh, H. Yamawaki, M. Sakashita, S. Takeya and K. Honda, Incommensurate composite crystal structure of scandium-II, *Phys. Rev. B: Condens. Matter Mater. Phys.*, 2005, **72**(13), 132103.
25 S. Arapan, N. V. Skorodumova and R. Ahuja, Determination of the structural parameters of an incommensurate phase from first principles: The case of Sc-II, *Phys. Rev. Lett.*, 2009, **102**(8), 85701.
26 I. Loa, R. J. Nelmes, L. F. Lundegaard and M. I. McMahon, Extraordinarily complex crystal structure with mesoscopic patterning in barium at high pressure, *Nat. Mater.*, 2012, **11**(7), 627–632.
27 S.-D. Huang, C. Shang, X.-J. Zhang and Z.-P. Liu, Material discovery by combining stochastic surface walking global optimization with a neural network, *Chem. Sci.*, 2017, **8**(9), 6327–6337.
28 P.-L. Kang, C. Shang and Z.-P. Liu, Large-scale atomic simulation via machine learning potentials constructed by global potential energy surface exploration, *Acc. Chem. Res.*, 2020, **53**(10), 2119–2129.
29 C. Shang and Z.-P. Liu, Stochastic surface walking method for structure prediction and pathway searching, *J. Chem. Theory Comput.*, 2013, **9**(3), 1838–1845.
30 C. Shang, X.-J. Zhang and Z.-P. Liu, Stochastic surface walking method for crystal structure and phase transition pathway prediction, *Phys. Chem. Chem. Phys.*, 2014, **16**(33), 17845–17856.
31 X.-J. Zhang and Z.-P. Liu, Variable-cell double-ended surface walking method for fast transition state location of solid phase transitions, *J. Chem. Theory Comput.*, 2015, **11**(10), 4885–4894.
32 S. Huang, C. Shang, P. Kang, X. Zhang and Z. Liu, LASP: Fast global potential energy surface exploration, *Wiley Interdiscip. Rev.: Comput. Mol. Sci.*, 2019, **9**(6), 1–11.
33 S. Zhu and Q. Hu, Unraveling the structural transition mechanism of room-temperature compressed graphite carbon, *Phys. Chem. Chem. Phys.*, 2021, **23**(36), 20560–20566.
34 S. Zhu, X. Yan, J. Liu, A. R. Oganov and Q. Zhu, A revisited mechanism of the graphite-to-diamond transition at high temperature, *Matter*, 2020, 1–15.
35 G. Kresse and J. Furthmüller, Efficient iterative schemes for *Ab Initio* total-energy calculations using a plane-wave basis set, *Phys. Rev. B: Condens. Matter Mater. Phys.*, 1996, **54**(16), 11169.
36 P. E. Blöchl, Projector augmented-wave method, *Phys. Rev. B: Condens. Matter Mater. Phys.*, 1994, **50**(24), 17953–17979.
37 J. P. Perdew, K. Burke and M. Ernzerhof, Generalized gradient approximation made simple, *Phys. Rev. Lett.*, 1996, **77**(18), 3865–3868.
38 H. J. Monkhorst and J. D. Pack, Special points for Brillouin-zone integrations, *Phys. Rev. B: Solid State*, 1976, **13**(12), 5188–5192.
39 X.-J. Zhang, C. Shang and Z.-P. Liu, Pressure-induced silica quartz amorphization studied by iterative stochastic surface walking reaction sampling, *Phys. Chem. Chem. Phys.*, 2017, **19**(6), 4725–4733.
40 D. J. Wales, Energy landscapes, in *Atomic clusters and nanoparticles. Agregats atomiques et nanoparticules*, Springer Berlin Heidelberg, Berlin, Heidelberg, 2001, pp. 437–507.
41 S.-C. Zhu, X.-Z. Yan, S. Fredericks, Y.-L. Li and Q. Zhu, First-principles investigation of Sc-III/IV under high pressure, *Phys. Rev. B*, 2018, **98**(21), 214116.
42 P. Tsuppayakorn-aek, W. Luo, W. Pungtrakoon, K. Chuenkingkeaw, T. Kaewmaraya, R. Ahuja and T. Bovornratanaraks, The ideal commensurate value of Sc and the superconducting phase under high pressure, *J. Appl. Phys.*, 2018, **124**(22), 225901.
43 J. Whaley-Baldwin, M. Hutcheon and C. J. Pickard, Superconducting incommensurate host-guest phases in compressed elemental sulfur, *Phys. Rev. B*, 2021, **103**(21), 1–10.
44 S.-C. Zhu, S.-H. Guan, W.-N. Zhao and Z.-P. Liu, Atomic structure of heterophase junction from theoretical prediction, *Top. Catal.*, 2015, **58**(10–11), 644–654.
45 S.-C. Zhu, S.-H. Guan and Z.-P. Liu, Mechanism and microstructures in Ga_2O_3 pseudomartensitic solid phase transition, *Phys. Chem. Chem. Phys.*, 2016, **18**(27), 18563–18574.